

# Bridging Theory and Experiment in Virtually Imaged Phased Array (VIPA) Spectrometers

Kiumars Aryana<sup>1,2,3,✉</sup>, D. Michelle Bailey<sup>1</sup>, Solomon I. Woods<sup>2</sup>, and Adam J. Fleisher<sup>1,✉</sup>

<sup>1</sup>Material Measurement Laboratory, National Institute of Standards and Technology, Gaithersburg, MD 20899, USA

<sup>2</sup>Physical Measurement Laboratory, National Institute of Standards and Technology, Gaithersburg, MD 20899, USA

<sup>3</sup>Department of Chemistry and Biochemistry, University of Maryland, College Park, MD 20742, USA

✉kiumars.aryana@nist.gov

✉adam.fleisher@nist.gov

## ABSTRACT

Virtually imaged phased array (VIPA) spectrometers provide high resolution and fast acquisition in a compact design, but their performance as dispersive instruments is sensitive to fabrication tolerances, component dimensions, and alignment. Here, leveraging numerical simulations validated by experimental data, we present a framework to identify the parameters that limit VIPA spectrometer resolution. This framework is applied to the construction of a new mid-infrared VIPA spectrometer, tested at wavelengths near  $\lambda = 4.6 \mu\text{m}$  with both continuous-wave and frequency-comb laser sources, with a resolving power predicted by analytical expressions to be as high as  $RP = 830\,000$  (corresponding to a resolution of  $\delta\nu = 78 \text{ MHz}$ ). Validated numerical simulations, however, provided a more realistic estimate that captures limits set by all the optical components. By correcting aberrations and optimizing alignment, a resolving power of  $RP = 440\,000$  ( $\delta\nu = 150 \text{ MHz}$ ) was experimentally achieved, corresponding to 80% of the value predicted by numerical simulation of the entire spectrometer. These results bridge the gap between analytical design expressions and experimental results for compact, high-resolution VIPA spectrometers to enable more efficient fabrication and advanced design across critical areas like applied space optics, line-by-line pulse shaping, and broadband spectral sensors.

## 1 Introduction

The unambiguous detection of multiple molecular species has vast applications in scientific research and industry, including for medical diagnostics<sup>1–3</sup> and imaging<sup>4</sup>, chemical kinetics<sup>5–7</sup>, plasma diagnostics<sup>8–11</sup>, and astronomical discoveries<sup>12,13</sup>. Different spectroscopic techniques offer trade-offs in terms of their spectral range, resolution, measurement speed, and size. Fourier Transform Infrared (FTIR) spectroscopy is one of the most widely used techniques, noted for its broad spectral coverage and commercial availability<sup>14,15</sup>. However, FTIR relies on moving components and its resolution is dependent upon the interferometer path length (with the exception being sub-nominal techniques<sup>16</sup>), a dimension which increases at longer wavelengths. An alternative approach that offers high resolving power ( $RP > 10^5$ ), albeit over a narrower spectral range, but eliminates the need for moving parts is the virtually imaged phased array (VIPA) spectrometer<sup>17</sup>. These instruments spatially disperse broadband light into its constituent wavelengths on a two-dimensional detector plane using orthogonal dispersive elements: a tilted Fabry–Pérot interferometric device (i.e., a VIPA) and a diffraction grating. At the heart of the spectrometer, the VIPA serves as the primary high-dispersion element, enabling a simple and compact spectrometer design.

The VIPA, developed for wavelength demultiplexing<sup>18–20</sup>, was first used in a cross-dispersed spectrometer for molecular fingerprinting in the visible at a wavelength of  $\lambda = 633 \text{ nm}$ <sup>17</sup>. That pioneering experiment achieved a resolving power of  $RP = 400\,000$  (based on a full-width at half-maximum (FWHM) definition<sup>21</sup> and the observed instrument line shape), which is about a factor of three shy of the VIPA-limited resolution predicted using an idealized model and assuming several key parameters for the etalon (see table 1). A subsequent demonstration of a VIPA spectrometer in the near-infrared achieved  $RP = 230\,000$  for molecular composition and breath analysis<sup>2</sup>, with a design having potential  $RP = 580\,000$  based on the detailed consideration of numerous optical components<sup>22</sup>. The first mid-infrared VIPA spectrometer reported  $RP = 130\,000$ <sup>23</sup>, lower than the VIPA-limited prediction of  $RP = 390\,000$ . More recently, a far-infrared VIPA was fabricated with measured  $RP = 16\,300$  at  $\lambda = 116 \mu\text{m}$  and cryogenic ( $T = 4 \text{ K}$ ) temperature<sup>24</sup>, with a corresponding VIPA-limited  $RP = 22\,000$ . The key parameters from these initial VIPA spectrometers are summarized in Table 1 to illustrate the challenges in achieving resolution limits when implementing proof-of-principle devices and instruments in new measurement regimes.

Numerical simulations offer a powerful tool to bridge the gap between analytical expressions for VIPA-limited resolving power and experimental observations of newly realized spectrometers. Furthermore, computational models allow for the controlled variation of parameters and components that are difficult or time-consuming to adjust experimentally. Therefore,

verified numerical simulations can enable high-performing VIPA spectrometers when utilized early in the design and testing phase. In this context, comprehensive system-level modeling is crucial—not only for design optimization but also for evaluating sensitivity, reducing prototyping, and predicting performance under different operating conditions.

**Table 1.** Informative summary of parameters found in the literature for the first reported virtually imaged phased array (VIPA) spectrometers in the visible, near-infrared, mid-infrared, and far-infrared spectral regions. These include wavelength ( $\lambda$ ), highly reflective (HR) coating power reflection coefficient ( $R_1$ ), partially reflective (PR) coating power reflection coefficient ( $R_2$ ), VIPA thickness ( $t$ ), incident beam angle ( $\theta_i$ ), and spacer material refractive index ( $n_r$ ). Also listed are the experimental (Exp.) and theoretical (Theo., based on analytical expressions<sup>25</sup>) resolving powers ( $RP$ ) and their ratio.

Study	$\lambda$ ( $\mu\text{m}$ )	$R_1$ (%)	$R_2$ (%)	$t$ (mm)	$\theta_i$ ( $^\circ$ )	$n_r$	Exp. $RP$	Theo. $RP$	Exp./Theo.
Diddams et al. <sup>17</sup>	0.633	100*	96	2*	2*	1.5*	400 000	1 400 000	29
Thorpe et al. <sup>2,22</sup>	1.6	100	96	1.5	2	2	230 000	580 000	40
Nugent-Glandorf et al. <sup>23</sup>	3.8	99.8	98	0.8	15	3.43	130 000	390 000	33
Zou et al. <sup>24†</sup>	115.7	99	92	9.9	13	3.39	16 300	22 000	74

\* Values for these parameters were not reported by Diddams et al.<sup>17</sup>. The values listed here are estimated to achieve a VIPA free spectral range of  $\nu_{\text{fsr}} = 50$  GHz, assuming a solid glass spacer and a small incident beam angle.

† Information from Zou et al.<sup>24</sup> is taken from their Table 1 and Figure 2 for a VIPA operating at a temperature of 4 K, where VIPA spacer material absorption losses are negligible.

In this work, we performed a systematic analysis to assess the impact of each optical component within a new mid-infrared VIPA spectrometer assembly, aiming to identify the critical factors contributing to instrument line shape broadening and distortion. Using analytical expressions, we calculated a theoretical resolving power for our VIPA spectrometer at  $\lambda = 4.6$   $\mu\text{m}$  of  $RP = 830 000$ . Through numerical simulation, we identified spherical aberration, imaging lens alignment, and aperture effects as the primary sources of resolution loss during initial spectrometer alignment. By addressing these initial deficiencies, we demonstrated that the spectrometer resolving power can be as high as  $RP = 440 000$ , thereby gaining a better understanding of the discrepancy between analytical expression predictions and experimental results at the component level.

The paper is organized as follows. The VIPA-limited resolving power is calculated in Section 2 using analytical expressions<sup>25</sup> to verify idealized numerical simulations and identify component limitations. We report an experimentally measured resolving power for the new cross-dispersed spectrometer in Section 3 using a continuous-wave quantum cascade laser (QCL) source and compare it to numerical simulations performed with realistic optical components and manufacturer-specified parameters. The resolving power is improved in Section 4, approaching the limit predicted by our more realistic numerical simulations. The VIPA angular dispersion is measured in Section 5 and compared with realistic numerical simulations. In Section 6, individual comb modes from a mid-infrared laser frequency comb source with repetition rate  $f_{\text{rep}} = 250$  MHz are resolved by the spectrometer. Finally, in Section 7, the VIPA optical throughput is measured and, through numerical simulations, excess losses (absorption and scattering) in the VIPA partially reflective coating are correlated with optical throughput.

## 2 VIPA Resolving Power in the Ideal Limit

Like a Fabry-Pérot interferometer, a VIPA consists of two reflective surfaces: one with a highly reflective (HR) coating and the other with a partially reflective (PR) coating. For a VIPA, however, light enters at a non-normal angle of incidence through an anti-reflective (AR) coated window and undergoes multiple displaced reflections inside the resonator, forming a series of virtual sources at the output PR face as illustrated in Fig.1(a). Interference between these virtual sources results in high angular dispersion, often exceeding that of a conventional diffraction grating and making VIPAs an effective element for high-resolution spectroscopy.

VIPA performance depends on 1) its design parameters like thickness, coating reflectivity, coating absorption, size, and spacer refractive index; 2) the quality of fabrication, such as surface flatness, parallelism, coating uniformity, and material purity; and 3) the precision of alignment, including the input beam angle of incidence, focusing conditions, and lens positioning.

### 2.1 Analytical Expressions vs. Numerical Simulations

The VIPA was tested prior to assembly of the cross-dispersed spectrometer by modeling the injection of a line-focused continuous-wave (CW) laser beam and monitoring the computed VIPA output as imaged by a spherical lens onto a detector array. A series of bright spots were observed, as illustrated by the red dots shown at the detector plane in Fig.1(a). The VIPA-limited line shape of the individual red dots is a Lorentzian function, and their relative intensity is defined by a Gaussian envelope as illustrated in Figs.1(a,b). The normalized intensity profile of the VIPA output under ideal conditions is calculated using the formalism proposed by Xiao et al.<sup>25</sup>, in which the normalized intensity profile is expressed as shown below in Eq. (1).

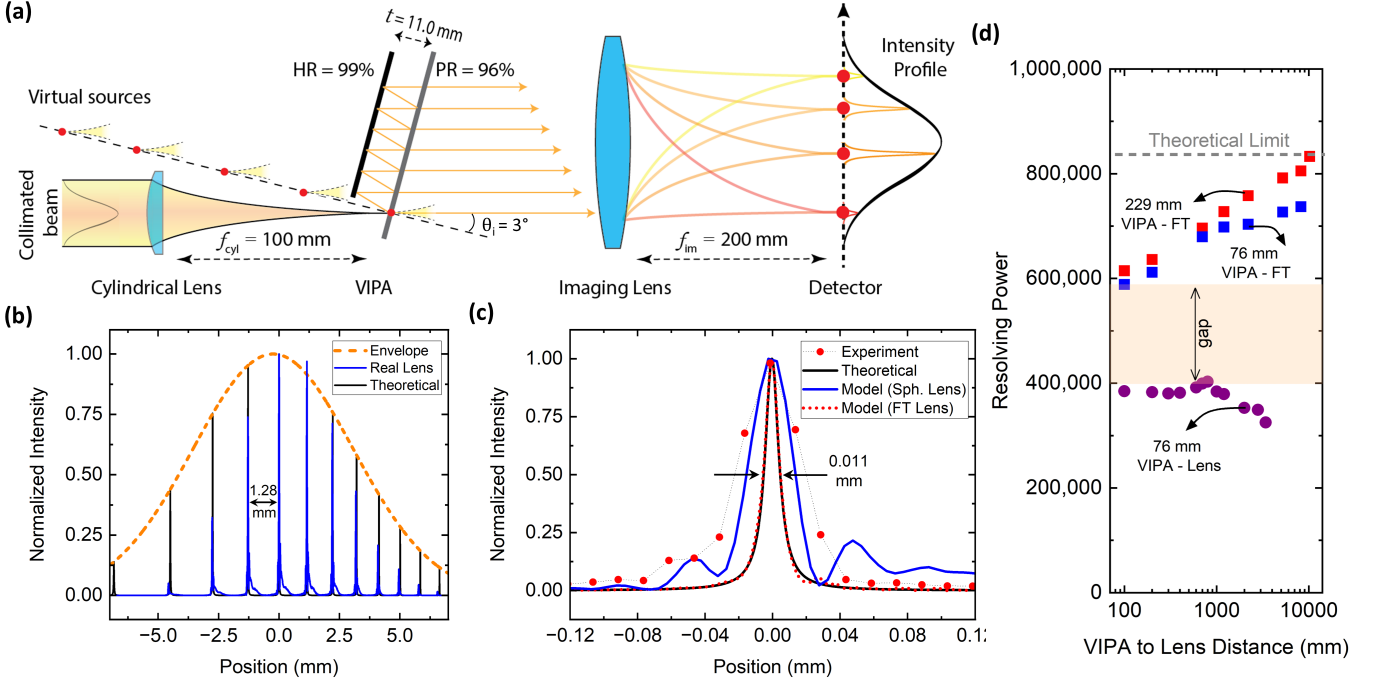


**Figure 1.** (a) Schematic of virtually imaged phased array (VIPA) spectral disperser and the underlying operation mechanism. (b) Comparison of VIPA outputs for the “idealized” analytical model and “realistic” numerical simulations. (c) A magnified view of (b), highlighting the ideal Lorentzian line shapes based on both analytical expressions and ray-tracing numerical simulations. (d) Numerical simulation results showing the achievable resolution as a function of the VIPA–detector distance and VIPA height, comparing an ideal Fourier-transform (FT) case with a 200 mm focal length imaging lens.

$$I_{\text{norm}}(x_{\text{im}}, \lambda) = \exp\left(-2 \frac{f_{\text{cyl}}^2 x_{\text{im}}^2}{W^2 f_{\text{im}}^2}\right) \frac{(1 - r_1 r_2)^2}{(1 - r_1 r_2)^2 + 4(r_1 r_2) \sin^2(\frac{k\Delta}{2})} \quad (1)$$

In Eq. (1),  $\lambda$  is the wavelength,  $x_{\text{im}}$  is the vertical distance normal to the beam,  $f_{\text{cyl}}$  is the cylindrical lens focal length,  $f_{\text{im}}$  is the imaging lens focal length,  $W$  is the Gaussian input beam radius,  $r_1$  and  $r_2$  are the electric-field reflection coefficients for the HR and PR coatings (power reflection coefficients  $R_1 = r_1^2$  and  $R_2 = r_2^2$ ),  $k$  is the wavenumber, and

$$\Delta = 2t n_r \cos(\theta_{\text{in}}) - 2t \tan(\theta_{\text{in}}) \cos(\theta_i) \theta_\lambda - t \cos(\theta_{\text{in}}) \theta_\lambda^2 / n_r, \quad k = 2\pi/\lambda, \quad \theta_\lambda \approx x_{\text{im}}/f_{\text{im}}, \quad n_r \sin(\theta_{\text{in}}) = \sin(\theta_i)$$

where  $t$  is the VIPA thickness,  $\theta_i$  is the incident angle of the beam relative to the VIPA entrance window,  $\theta_{\text{in}}$  is the internal angle of reflection,  $\theta_\lambda$  is the output dispersion angle, and  $n_r$  is the refractive index of the VIPA spacer material. Note that VIPA spacer absorption losses are not considered here.

The mid-infrared VIPA tested here comprises highly and partially reflective coatings with manufacturer-specified power reflection coefficients  $R_1 = 99\%$  and  $R_2 = 96\%$ , respectively, separated by a  $\text{CaF}_2$  spacer<sup>26</sup> ( $n_r = 1.4036$ ) with a thickness of  $t = 11.0$  mm and height of  $l = 76.2$  mm. The VIPA was positioned where the collimated input beam radius was  $W = 3$  mm, and at a tilt angle of  $\theta_i = 3^\circ$ . The cylindrical and imaging lens focal lengths were 100 mm and 200 mm (215 mm wavelength-corrected effective focal length), respectively. Figure 1(b) shows the intensity profile of the VIPA output as imaged onto the detector. The spatial separation between peaks resulted from the VIPA nonlinear angular dispersion. Again, following Xiao et al.<sup>25</sup>, the VIPA free spectral range ( $\nu_{\text{FSR}}$ ) was calculated based on the VIPA thickness, spacer material, and angle of incidence by the following expression,

$$\nu_{\text{FSR}} = \frac{c}{\Delta} \approx \frac{c}{2n_r t \cos(\theta_{\text{in}})} \left\{ 1 + \tan(\theta_{\text{in}}) \theta_\lambda + \left[ \frac{1}{2} + (\tan)^2(\theta_{\text{in}}) \right] \theta_\lambda^2 \right\} \quad (2)$$

where the approximate portion of the expression was derived from a second-order Taylor series expansion of the quantity  $c/\Delta$  about the term  $\theta_{\text{in}}$ .

From the analytical expressions, we calculated  $v_{\text{FSR}} = 9.7$  GHz at a central wavelength of  $\lambda = 4.6 \mu\text{m}$ . From this, the resolving power was estimated by determining the number of peaks that fit within the vertical separation of two adjacent transmission maxima (one free spectral range), which is approximately 1.28 mm on the focal plane. Given a FWHM of 0.011 mm for an individual transmission peak in the ideal Fourier-transform case, up to 123 peaks can theoretically be resolved within a single free spectral range. This corresponded to a resolving power of  $RP = 830\,000$  at  $\lambda = 4.6 \mu\text{m}$ , which could allow the system to resolve Lorentzian peaks—based on the FWHM definition of resolving power<sup>21</sup>—as close as  $\delta v = 78$  MHz.

Resolving power can also be derived from scalar diffraction theory, which provides the analytical expression for spectral resolving power of the VIPA as

$$RP = \lambda \frac{F_R}{\lambda_{\text{FSR}}} \quad (3)$$

where  $F_R \approx \pi(R_1 R_2)^{1/4}/(1 - \sqrt{R_1 R_2})$  represents the finesse of the VIPA, and  $\lambda_{\text{FSR}}$  is the free spectral range expressed in wavelength domain. This calculation yielded a resolving power of approximately 830 000, consistent with the earlier estimate based on the number of peaks that fit within one free spectral range.

## 2.2 Numerical Simulations vs. Experimental Results

To obtain a more accurate estimate of the resolving power, numerical simulations were performed on the VIPA assembly without the grating, including parameters like VIPA reflection and transmission as well as refraction through the cylindrical and imaging lenses. For this purpose, a non-sequential ray tracing approach was implemented in Zemax OpticStudio<sup>27</sup> to accurately simulate complex light propagation, including multiple reflections and beam overlap within the VIPA and imaging system. Optical components such as lenses were modeled using manufacturer-provided specifications, while the VIPA was built by pairing highly and partially reflective surfaces, separated by a CaF<sub>2</sub> spacer. Absorption and scattering losses were neglected in the VIPA coatings, and simulations were performed using one million rays. The detector was placed at the focal plane of the imaging lens, and its position was fine-tuned to minimize the simulated VIPA transmission linewidth. The modeled detector array specifications matched those of the infrared camera used in the experimental evaluation, with an array size of 640 pixels by 512 pixels and a pixel pitch of 15  $\mu\text{m}$ .

Compared in Fig. 1(b,c) are calculations made using the analytical expression and the results of the numerical simulations, with a zoomed-in trace also shown in Fig. 1(c). For comparison, an experimental measurement of transmission peaks from the VIPA output is shown (see Sections 3–4). The analytical expression in the paraxial limit (solid black line) represents the ideal case and produces the narrowest FWHM and thus defines the theoretical VIPA-limited resolving power. In contrast, the ray-tracing numerical simulation (solid blue line) incorporated both intrinsic and extrinsic contributions, and yielded a broader linewidth of 0.026 mm—more than a factor of two larger than that modeled by the analytical expressions.

The discrepancy between the analytical expressions and numerical simulations is understood by systematically varying the optical component parameters within the numerical simulation. The dominant factors found to influence the resolving power in the numerical simulations were 1) the VIPA height, 2) aberrations introduced by the imaging lens, 3) aperture effects, and 4) the positioning of the imaging lens relative to the VIPA. Several of these extrinsic limitations were eliminated in the numerical simulations by applying a Fourier transform to the VIPA electric field transmission, which effectively simulates an “idealized lens.” As shown in Fig. 1(c,d) by the red dotted line, the idealized lens approach improved agreement between the numerical simulation and analytical expression results. This is also illustrated in Fig. 1(d): at a detector distance of approximately 400 mm, the resolving power reached 623 000 for an idealized lens with a sufficiently tall ( $l = 228.6$  mm) VIPA which captured a large number of internal reflections (compared to 577 000 for the VIPA with  $l = 76.2$  mm used in the experiment). However, when a lens with diameter  $D = 50.8$  mm was used in the simulation instead of the Fourier transform, the resolving power dropped significantly to 360 000. The reduced resolving power is attributed to imaging lens aberrations, the reduced aperture, and the continued beam divergence that prevented the smaller-diameter lens from collecting a sufficient fraction of the full VIPA transmission.

Overall, this section demonstrates that numerical simulations can effectively bridge the gap between theoretical predictions and practical experiments. The results show in the specific case studied here, increasing the VIPA height and employing aberration-free lenses can significantly enhance spectrometer performance, thereby reducing the gap between VIPA-limited theoretical predictions from analytical expressions and practical realizations based on numerical simulations. It should be noted that the minimum VIPA height depends strongly on the reflectivity of the PR and HR surfaces as well as the angle of incidence<sup>28</sup>; for lower reflectivities or steeper incidence angles, a height of 228.6 mm may be sufficient to capture all internal reflections. In the next section, this approach is extended to the full cross-dispersed spectrometer assembly with grating and

numerical simulations are again used to identify the key parameters responsible for deviations from VIPA-limited theoretical performance.

### 3 Cross-Dispersed Spectrometer: Initial Experimental Results

The previous section showed that numerical simulations can bridge the gap between predictions by analytical expressions and experimental observations. Here we extend the numerical simulations to a full cross-dispersed spectrometer and present the initial measured resolving power for the mid-infrared VIPA spectrometer.

The experimental setup is shown in Fig. 2(a,b). It includes a fiber collimator with free-space output beam (radius of  $W = 3$  mm) that was line-focused by a cylindrical lens of  $f_{\text{cyl}} = 100$  mm. The VIPA specifications were previously listed in Section 2 and shown in Fig. 1. The VIPA output was directed at a diffraction grating with a groove number of  $300 \text{ mm}^{-1}$ , and the first-order output from the grating was collected using a flat mirror and then focused onto the detector array and camera by an imaging lens with  $f_{\text{im}} = 200$  mm (215 mm wavelength-corrected effective focal length). The camera had a  $15 \mu\text{m}$  pixel pitch, an array size of 640 pixels by 512 pixels, a spectral response range from  $\lambda = 1.5 \mu\text{m}$  to  $\lambda = 5.1 \mu\text{m}$ , an integration time of 500  $\mu\text{s}$ , and a frame rate of 100 Hz.

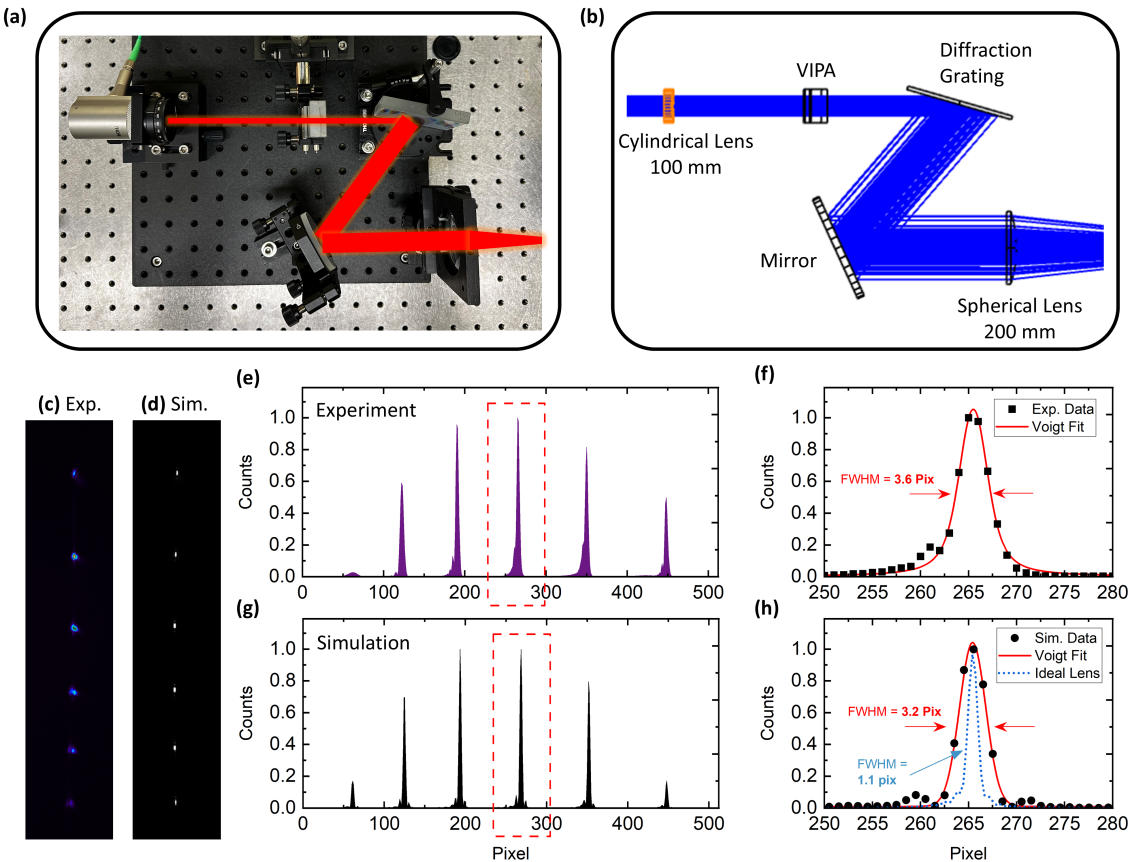


**Figure 2.** (a) Experimental setup and (b) layout for numerical simulation. (c,d) Detector images from experiment and simulation. (e,g) Cross-sectional profiles of the 2D images highlighting Lorentzian linewidth. (f,h) Zoomed-in view of the central peak with the corresponding Lorentzian fit.

The detector images at a wavelength of  $4.6 \mu\text{m}$  are shown in Fig. 2(c,d) for both the experimental measurement and the numerical simulation. The corresponding cross-sectional line profiles of the peaks are presented in Figs. 2(e,g), while a magnified view of the central peaks fitted to Lorentzian functions are provided in Figs. 2(f,h). (Note that fitting to more advanced line shape functions<sup>29</sup>, including convolutions of multiple functions<sup>30</sup>, is not the focus of this work.) From these Lorentzian fits, the FWHM values were 3.2 pixels for the experiment and 2.2 pixels for the simulation. In Figs. 2(e,g), the peak spacing spanned approximately 98 pixels, sufficient space to accommodate  $\approx 30$  (experiment) and  $\approx 44$  (simulation) peaks within one free spectral range. The corresponding resolving powers are  $RP = 200\,000$  (experiment) and  $RP = 270\,000$

(numerical simulation) for a VIPA tilt angle of  $3^\circ$ . As will be shown in the next section, the numerical simulation suggests that a smaller tilt angle like  $1.5^\circ$  would achieve an improved resolving power as high as  $RP = 400\,000$ . Furthermore, when a Fourier transform is applied to remove aberration effects, the Lorentzian linewidth narrows to 1.2 pixels, corresponding to an idealized full-instrument resolving power of up to 570 000.

## 4 Cross-Dispersed Spectrometer: Experimental Optimization

For optimizing the alignment, the imaging lens and grating height were adjusted to maximize the collection of light emerging from the VIPA. To mitigate spherical aberration, a lens with a longer focal length was used. Since a longer focal length corresponds to a larger radius of curvature at a fixed lens diameter, aberrations were reduced when the lens f-number was increased (where the lens f-number is  $F = f_{\text{im}}/D$ , and  $D$  is the lens diameter). To demonstrate this effect, we compared experimental results obtained using an imaging lens with  $f_{\text{im}} = 1000$  mm ( $F = 20$ ) to another with  $f_{\text{im}} = 200$  mm ( $F = 4$ ). As shown in Fig. 3, the resolving powers achieved with the 200 mm and 1000 mm lenses are  $RP = 290\,000$  and  $RP = 440\,000$ , respectively. The longer focal length imaging lens also made better use of the detector array by magnifying the image and stretching one free spectral range over more pixels. These results underscore the critical role of the imaging lens in achieving VIPA-limited spectrometer performance and suggest that an aberration-free imaging lens with a large f-number would enable enhanced resolving power.

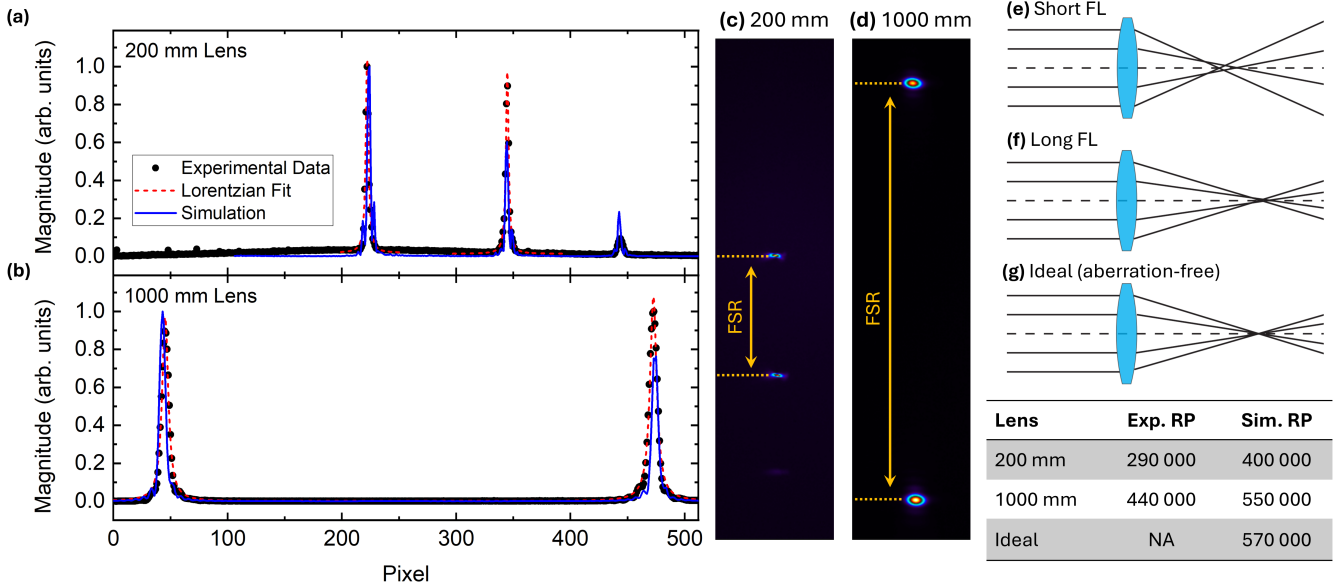


**Figure 3.** The effect of imaging lens focal length at fixed lens diameter on the VIPA resolving power. Numerical simulations (blue lines) were performed with (a)  $f_{\text{im}} = 200$  mm and (b)  $f_{\text{im}} = 1000$  mm imaging lenses and are compared to experimental results (red dashed lines). Peaks from the VIPA output were compared for both the numerical simulations and experiments for (c)  $f_{\text{im}} = 200$  mm and (d)  $f_{\text{im}} = 1000$  mm. (e-g) Schematics of spherical aberration from short focal-length, long focal-length, and ideal aberration-free lenses. The experimental resolving powers achieved are listed in the table in the image, along with corresponding values from numerical simulations.

## 5 VIPA Angular Dispersion

The VIPA angular dispersion determines how well different frequencies of light are resolved at the detector. In this section, we demonstrate how the dispersion characteristics of the VIPA can be numerically simulated to verify experimental results, providing practical guidance for optimizing spectrometer design and alignment. A schematic of the VIPA angular dispersion is presented in Fig. 4(a), where each peak corresponds to a distinct wavelength. Here, the laser wavelength was tuned by adjusting the QCL temperature, with a tuning coefficient  $\approx 0.43 \text{ nm K}^{-1}$  determined via curve fitting of the transmission from a commercial silicon etalon. As the wavelength was adjusted, the position of the transmission peak shifted across the two-dimensional detector plane.

Figure 4(a-i-iv) shows camera images captured as the QCL wavelength was incrementally increased from 4600.0 nm to 4602.5 nm. Due to the VIPA angular dispersion, increases in the laser wavelength manifested as changes in the dispersion output

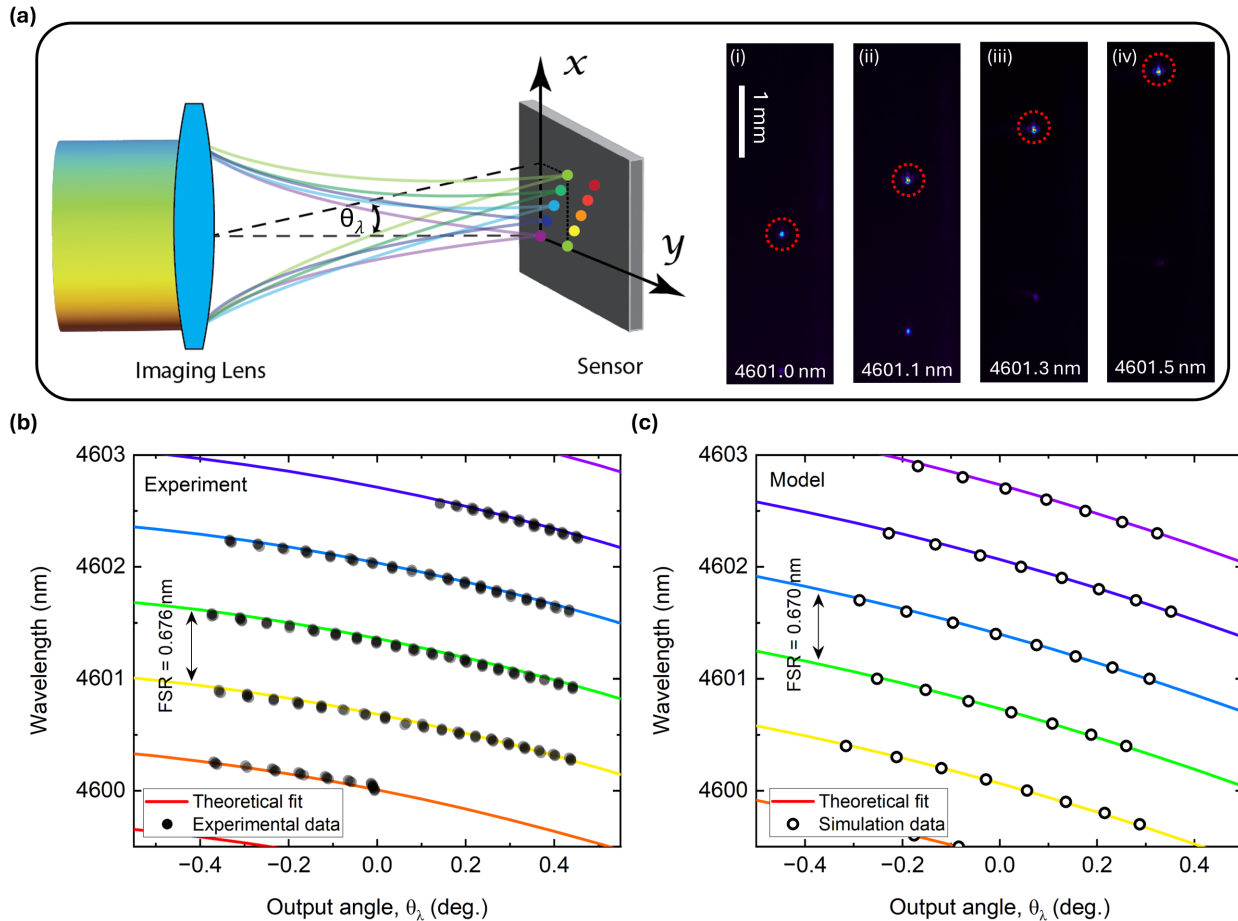


**Figure 4.** (a) Schematic of the angular dispersion measurement, along with the detector image captured for wavelengths ranging from (i) 4601.0 nm to (iv) 4601.5 nm. (b, c) Experimental and numerical simulation results show the laser wavelength as a function of the VIPA output angle, overlaid with the corresponding fit based on Eq. (4).

angle and the motion of the transmission peaks in the plane of the detector array. The output angle ( $\theta_\lambda$ ) was estimated from the vertical displacements of the peak positions ( $x_{\text{im}}$ ) on the image plane and the focal length of the imaging lens ( $f_{\text{im}}$ ) using the small angle approximation  $\theta_\lambda = \arctan(x_{\text{im}}/f_{\text{im}}) \approx x_{\text{im}}/f_{\text{im}}$ . The solid circles in Fig. 4(b) represent the experimentally measured VIPA output angle as a function of laser wavelength, while the open circles in Fig. 4(c) show the corresponding results from the numerical simulations. The angular dispersion can also be analytically determined using the paraxial approximation of Xiao et al.<sup>25</sup>, which relates wavelength to output angle via the following equation,

$$\Delta\lambda = \lambda_p - \lambda_0 = -\lambda_0 \left[ \frac{\tan(\theta_{in}) \cos(\theta_i)}{\cos(\theta_m)} \frac{\theta_\lambda}{n_r} + \frac{1}{2} \frac{\theta_\lambda^2}{n_r^2} \right] \quad (4)$$

where  $\lambda_0 = \frac{2\pi}{m} \cos(\theta_m)$ . For this measurement, the incident angle of the VIPA was set to  $\approx 1.5^\circ$ . The separation of the repeating curves observed in Fig. 4(b, c) corresponds to the VIPA free spectral range, which defines the wavelength spacing between adjacent VIPA orders. The free parameters in the fit are the center wavelength and the FSR. Within each FSR, the output angle varied approximately from  $-0.4^\circ$  to  $0.4^\circ$ , yielding an angular dispersion of  $\approx 1.2^\circ \text{nm}^{-1}$ . When compared to calculations from the analytical expressions, we determined  $\lambda_{\text{FSR}} = 0.676 \text{ nm}$  from the experimental data and  $\lambda_{\text{FSR}} = 0.670 \text{ nm}$  from the numerical simulations. These values are nearly equal to the value predicted by the analytical expression of  $\lambda_{\text{FSR}} = 0.686 \text{ nm}$ , deviating by only approximately 1% and 2%, respectively.

## 6 Laser Frequency Comb Resolved

This section describes the use of a laser frequency comb source with a repetition rate of  $f_{\text{rep}} = 250 \text{ MHz}$  to test the broadband resolving capabilities of our new VIPA spectrometer. At a central wavelength of  $4.6 \mu\text{m}$ , the comb source mode spacing corresponded to approximately 17 pm, which required a FWHM resolving power of at least 260 000. The previous section showed that the system—with the 1000 mm focal length—would reach resolving powers as high as 440 000, suggesting that the spectrometer should resolve adjacent comb modes.

Figure 5 shows a comparison between experimental measurements and numerical simulations of the VIPA spectrometer illuminated by the laser frequency comb source. The experimental two-dimensional spectrogram captured by the mid-infrared camera is shown in Fig. 5(a). Individual comb modes are clearly resolved along the vertical VIPA dispersion dimension, highlighted in the figure by a red dashed, overlaid box. This box also highlights the portion of the image extracted for further quantitative analysis and illustrated in Figs. 5(b,c). In Fig. 5(b), the raw intensity profile shows comb modes appearing as a series of peaks separated by  $14.5 \pm 0.9$  pixels. Figure 5(c) shows the same profiles but normalized, from which we extract an average FWHM of  $7.1 \pm 1.4$  pixels using fits to a series of Lorentzian functions.

The experimental results are validated by comparison to numerical simulations found in Figs. 5(d–f). The simulated image is shown in Fig. 5(d), again with the extracted slice marked by the red dashed, overlaid box. The slice is shown in Fig. 5(e,f), with peaks spaced by  $11.6 \text{ pixels} \pm 1.2 \text{ pixels}$ . Fits to Lorentzian functions yielded an average FWHM of  $5.7 \text{ pixels} \pm 0.8 \text{ pixels}$ . Although the absolute pixel values differ slightly from experiment, the overall agreement between experimental and numerically simulated results was good. Importantly, both approaches confirmed that the spectrometer can resolve frequency comb modes spaced by 250 MHz.

These comb mode resolved results directly demonstrate the improved precision of cross-dispersed spectrometer for mid-infrared spectroscopy. The correspondence between experiment and numerical simulation highlights the robustness of our computer modeling framework, which was used to refine system parameters, inform optimized alignment, and predict performance under alternative configurations. The ability to simulate full spectrometer performance increased confidence in the design and enabled the development of higher precision spectrometers.

## 7 VIPA Optical Throughput and Coating Excess Loss

Finally, the numerical simulations enabled an evaluation of the VIPA optical throughput. The optical throughput of the VIPA was defined by the coating reflectivity, transmission, and absorption plus scattering (excess) losses. Figure 6 presents the numerically simulated optical throughput of the VIPA as a function of coating absorption losses at the PR surface (assuming zero scattering) based on the model discussed earlier in Fig 1, with the reflectivities of both mirrors held constant and assuming no excess losses at the AR-coated input window or the HR coating. In these numerical simulations, only the absorption of the PR surface was varied. The results revealed a linear trend, where increased absorption losses at the PR face resulted in decreased optical throughput.

We experimentally measured the optical power throughput of our VIPA using a lens with a focal length of 200 mm to collect most of the transmitted laser light and focus it onto a thermal power meter. The measured power throughput was approximately 60% of the input laser power. As shown in Fig. 6, the numerically simulated ideal case—where the PR surface has no absorption

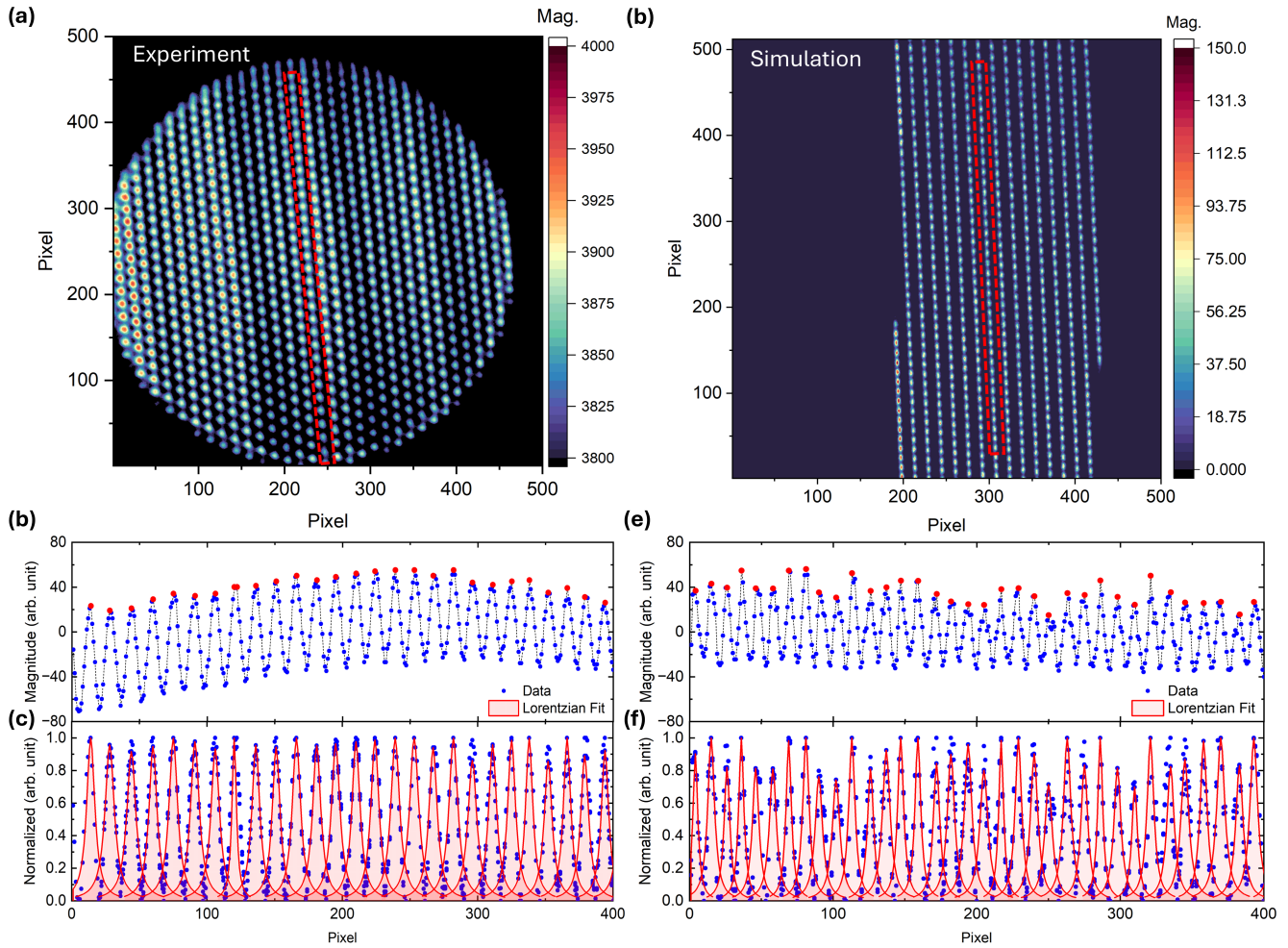


**Figure 5.** The mid-infrared VIPA spectrometer under frequency-comb illumination. (a) Experimental two-dimensional spectrogram showing broadband spectrometer output; the red dashed line marks an extracted region for analysis. (b–c) Experimental line-out along the boxed region: (b) raw intensity profile with individual frequency-comb modes (red dots), (c) normalized peak profiles fitted with Lorentzian functions, yielding an average FWHM of  $7.1 \text{ pixels} \pm 1.4 \text{ pixels}$  and a mean peak spacing of  $14.5 \text{ pixels} \pm 0.9 \text{ pixels}$ . (d) Numerically simulated spectrogram under equivalent conditions. (e–f) Numerical simulation line-out: (e) raw intensity profile with detected peaks, (f) normalized peak profiles fitted with Lorentzian line-shape functions, yielding an average FWHM of  $5.7 \text{ pixels} \pm 0.8 \text{ pixels}$  and a mean peak spacing of  $11.6 \text{ pixels} \pm 1.2 \text{ pixels}$ .

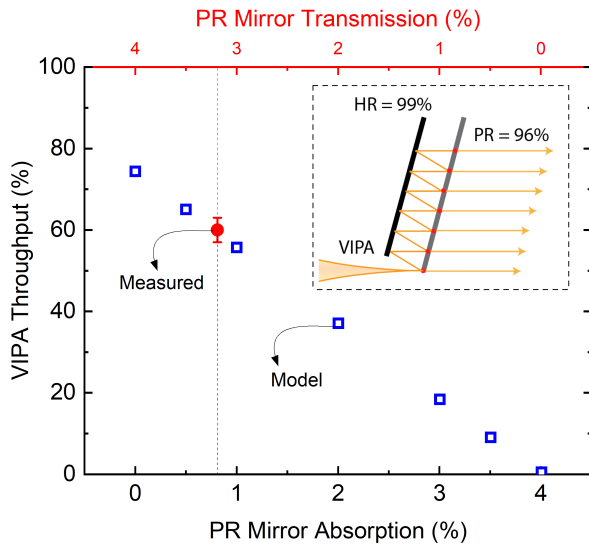


**Figure 6.** VIPA optical throughput ( $P_{\text{out}}/P_{\text{in}}$ ) at  $\lambda = 4.6 \mu\text{m}$  as a function of absorption in the partially reflective (PR) coating. The measured value for the device studied here is shown as a solid red circle, with error bars representing the standard deviation across four independent measurements. The transmission and absorption were not directly measured but were instead inferred from the numerical simulation. The reflectivities at both the HR and PR coatings were kept constant in the simulation, while only the absorption of the PR surface was varied.

and 4% transmission (96% reflectivity)—yielded a throughput near 75%. When the PR transmission was reduced to 2% due to absorption or scattering losses, the throughput dropped sharply to below 50%. By comparing the measured results with numerical simulations, we estimated that the PR surface transmission was approximately 3.2% and the absorption was about 0.8%. It should be noted that the transmission and absorption values were not measured directly; rather, they were inferred from simulations that best matched the experimental data. These results highlight the critical importance of minimizing absorption and employing high-quality, low-loss coatings in VIPA construction to maximize optical throughput.

## 8 Conclusion

In this work, we combined numerical simulations and experimental measurements to investigate the discrepancy between analytically predicted and experimentally observed resolving power in a virtually imaged phased array (VIPA) spectrometer. While the analytical expressions for the mid-infrared VIPA predicted a resolving power of  $RP = 830\,000$  at a wavelength of  $\lambda = 4.6 \mu\text{m}$ , the initial measurements yielded lower values by about a factor of four. Through systematic analysis, the VIPA length and spherical aberration from the imaging lens were identified as the dominant limiting factors. By employing a longer focal length imaging lens, the resolving power more than doubled to  $RP = 440\,000$ , and numerical simulations suggested values higher than  $RP = 570\,000$  would be possible with aberration-free optics and a taller VIPA structure. For the complete cross-dispersed spectrometer, the achieved resolving power corresponded to 80% of the limit determined by numerical simulations. The results serve to highlight the critical role of imaging lens choice and design, as well as VIPA length and geometry, in bridging the gap between analytical expressions and real observations and provide practical pathways toward designing and fabricating compact spectrometers with high resolution across the electromagnetic spectrum.

## References

1. Bacon, C. P., Mattley, Y. & DeFrece, R. Miniature spectroscopic instrumentation: Applications to biology and chemistry. *Rev. Sci. Instruments* **75**, 1–16 (2004).
2. Thorpe, M. J., Balslev-Clausen, D., Kirchner, M. S. & Ye, J. Cavity-enhanced optical frequency comb spectroscopy: application to human breath analysis. *Opt. Express* **16**, 2387–2397 (2008).
3. Liang, Q. *et al.* Breath analysis by ultra-sensitive broadband laser spectroscopy detects SARS-CoV-2 infection. *J. Breath Res.* **17**, 036001 (2023).

4. Desoutter, A. *et al.* VIPA based high-contrast high-efficiency two-stage Brillouin imaging spectrometer using a single diffraction mask. *J. Appl. Phys.* **138**, 044702 (2025).
5. Fleisher, A. J. *et al.* Mid-infrared time-resolved frequency comb spectroscopy of transient free radicals. *The J. Phys. Chem. Lett.* **5**, 2241–2246 (2014).
6. Bjork, B. J. *et al.* Direct frequency comb measurement of OD + CO → DOCO kinetics. *Science* **354**, 444–448 (2016).
7. Lucas, D. I., Guillaume, T., Heard, D. E. & Lehman, J. H. Design and implementation of a new apparatus for astrochemistry: Kinetic measurements of the CH + OCS reaction and frequency comb spectroscopy in a cold uniform supersonic flow. *The J. Chem. Phys.* **161**, 094203 (2024).
8. Sadiek, I., Lang, N., Fleisher, A. J. & van Helden, J.-P. Precision frequency comb spectroscopy of reactive molecular plasmas. In *CLEO 2024*, SF2F.6 (Optica Publishing Group, 2024).
9. Sadiek, I. *et al.* Dual-comb spectroscopy of ammonia formation in non-thermal plasmas. *Commun. Chem.* **7**, 110 (2024).
10. Sadiek, I., Lang, N. & Helden, J.-P. H. V. Air-spaced virtually imaged phased array with 94 MHz resolution for precision spectroscopy. *Opt. Express* **32**, 46511–46521 (2024).
11. Sadiek, I., Bernardo, S. D., Macherius, U. & van Helden, J.-P. H. Formation of HNC and HCN isomers in molecular plasmas revealed by frequency comb and quantum cascade laser spectroscopy. *arXiv* 2511.13519 (2025). [physics.chem-ph/2511.13519](https://arxiv.org/abs/2511.13519).
12. Zhu, X., Lin, D., Hao, Z., Wang, L. & He, J. A VIPA spectrograph with ultra-high resolution and wavelength calibration for astronomical applications. *The Astron. J.* **160**, 135 (2020).
13. Ferruit, P. *et al.* The Near-Infrared Spectrograph (NIRSpec) on the James Webb Space Telescope-II. Multi-object spectroscopy (MOS). *Astron. & Astrophys.* **661**, A81 (2022).
14. Griffiths, P. R. Fourier transform infrared spectrometry. *Science* **222**, 297–302 (1983).
15. Dutta, A. Chapter 4 - Fourier transform infrared spectroscopy. In Thomas, S., Thomas, R., Zachariah, A. K. & Mishra, R. K. (eds.) *Spectroscopic Methods for Nanomaterials Characterization*, Micro and Nano Technologies, 73–93 (Elsevier, 2017).
16. Maslowski, P. *et al.* Surpassing the path-limited resolution of fourier-transform spectrometry with frequency combs. *Phys. Rev. A* **93**, 021802 (2016).
17. Diddams, S. A., Hollberg, L. & Mbele, V. Molecular fingerprinting with the resolved modes of a femtosecond laser frequency comb. *Nature* **445**, 627–630 (2007).
18. Shirasaki, M. Large angular dispersion by a virtually imaged phased array and its application to a wavelength demultiplexer. *Opt. Lett.* **21**, 366–368 (1996).
19. Xiao, S. & Weiner, A. M. 2-D wavelength demultiplexer with potential for  $\geq 1000$  channels in the C-band. *Opt. Express* **12**, 2895–2902 (2004).
20. Wang, S. X., Xiao, S. & Weiner, A. M. Broadband, high spectral resolution 2-D wavelength-parallel polarimeter for Dense WDM systems. *Opt. Express* **13**, 9374–9380 (2005).
21. Robertson, J. G. Quantifying resolving power in astronomical spectra. *Publ. Astron. Soc. Aust.* **30**, e048 (2013).
22. Thorpe, M. *Cavity-enhanced direct frequency comb spectroscopy*. Ph.D. thesis, University of Colorado Boulder, Boulder (2009).
23. Nugent-Glandorf, L. *et al.* Mid-infrared virtually imaged phased array spectrometer for rapid and broadband trace gas detection. *Opt. Lett.* **37**, 3285–3287 (2012).
24. Zou, B. *et al.* Demonstration of a high-resolution virtually imaged phased array in the far-infrared. *Appl. Opt.* **64**, 3071–3082 (2025).
25. Xiao, S., Weiner, A. M. & Lin, C. A dispersion law for virtually imaged phased-array spectral dispersers based on paraxial wave theory. *IEEE J. Quantum Electron.* **40**, 420–426 (2004).
26. Malitson, I. H. A redetermination of some optical properties of calcium fluoride. *Appl. Opt.* **2**, 1103–1107 (1963).
27. Certain equipment, instruments, software, or materials are identified in this paper in order to specify the experimental procedure adequately. Such identification is not intended to imply recommendation or endorsement of any product or service by NIST, nor is it intended to imply that the materials or equipment identified are necessarily the best available for the purpose.

28. Born, M. *et al.* *Principles of Optics: Electromagnetic Theory of Propagation, Interference and Diffraction of Light* (Cambridge University Press, 1999), 7 edn.
29. Bailey, D. M. & Fleisher, A. J. Improved performance of a mid-infrared cross-dispersed comb spectrometer using a fast framerate InSb array. In *Optica Sensing Congress 2024 (AIS, LACSEA, Sensors, QSM)*, LM2D.2 (Optica Publishing Group, 2024).
30. Bailey, D. M., Zhao, G. & Fleisher, A. J. Precision spectroscopy of nitrous oxide isotopocules with a cross-dispersed spectrometer and a mid-infrared frequency comb. *Anal. Chem.* **92**, 13759–13766 (2020).

## Acknowledgment

All authors acknowledge funding from the National Institute of Standards and Technology (NIST). KA, SIW, and AJF acknowledge funding from the NIST IMS program. Work by AJF was also performed with funding from the CHIPS Metrology Program, part of CHIPS for America, NIST, U.S. Department of Commerce. All authors acknowledge Eisen Gross (NIST) and Kevin Cossel (NIST) for commenting on the manuscript.

## Author contributions

KA performed the numerical simulations. KA and DMB performed the experiments. KA, SIW, and AJF contributed to study methodology. SIW and AJF provided funding acquisition and project administration. AJF conceptualized the study. All authors contributed to writing the manuscript.

## Competing interests

The authors declare no competing interests.